JACS
JOURNAL OF THE AMERICAN CHEMICAL SOCIETY
pubs.acs.org/JACS
Communication

Nanoscale Metal–Organic Layers Detect Mitochondrial Dysregulation and Chemoresistance via Ratiometric Sensing of Glutathione and pH

Xiang Ling,[#] Deyan Gong,[#] Wenjie Shi, Ziwan Xu, Wenbo Han, Guangxu Lan, Youyou Li, Wenwu Qin, and Wenbin Lin*

Cite This: J. Am. Chem. Soc. 2021, 143, 1284–1289

ABSTRACT: Mitochondrial dysregulation controls cell death and survival by changing endogenous molecule concentrations and ion flows across the membrane. Here, we report the design of a triply emissive nanoscale metal–organic layer (nMOL), NA@Zr-BTB/F/R, for sensing mitochondrial dysregulation. Zr-BTB nMOL containing Zr_6 secondary building units (SBUs) and 2,4,6-tris(4-carboxyphenyl)aniline (BTB-NH_2) ligands was postsynthetically functionalized to afford NA@Zr-BTB/F/R by exchanging formate capping groups on the SBUs with glutathione(GSH)-selective (2*E*)-1-(2′-naphthyl)-3-(4-carboxyphenyl)-2-propen-1-one (NA) and covalent conjugation of pH-sensitive fluorescein (F) and GSH/pH-independent rhodamine-B (R) to the BTB-NH_2 ligands. Cell imaging demonstrated NA@Zr-BTB/F/R as a ratiometric sensor for mitochondrial dysregulation and chemotherapy resistance via GSH and pH sensing.

As the powerhouse of the cell, the mitochondrion exercises strict homeostatic control of many potentially harmful molecules.[1] Dysregulation of mitochondrial homeostasis can stop cell proliferation and elicit cell death.[2] Understanding the role of mitochondrial dysregulation in pathophysiological processes is important for the development of therapeutic strategies for many diseases, particularly chemoresistant cancers.[3,4] As an antioxidant for maintaining cellular redox homeostasis, glutathione (GSH) is synthesized in the cytosol and distributed into different subcellular compartments. The mitochondrion has the same GSH concentration as the cytosol.[5] As many cell death-inducing stimuli interact with mitochondria to cause oxidative stress,[6] mitochondrial GSH plays a critical role in maintaining a proper redox environment for cell survival.[7] While the pH value in normal mitochondria is known to be alkaline,[8] mitochondrial dysregulation impacts ion influx and generates a proton gradient across the mitochondrial membrane, lowering the pH in mitochondrial matrix.[9] Thus, the development of sensors for GSH and pH in mitochondria can reveal important insights into mitochondrial dysregulation and offer an opportunity to understand various pathophysiological processes such as chemoresistant cancers.

Built from metal-oxo cluster secondary building units (SBUs) and organic bridging ligands, nanoscale metal–organic frameworks (nMOFs) have been exploited for chemical and biological sensing applications.[10−25] However, the strict symmetry requirement of bridging ligands and small pores of nMOFs have hindered their multifunctionalization and limited their application in sensing large molecules. As a two-dimensional version of nMOFs, nanoscale metal–organic layers (nMOLs) not only retain the molecular tunability, structure regularity, compositional diversity of nMOFs but also possess high densities of open sites for multifunctionalization and detection of large analytes,[26] offering a versatile platform to design ratiometric sensors for multiple analytes in biological systems.

Herein, we report the design of an nMOL-based biosensor, NA@Zr-BTB/F/R, for ratiometric GSH and pH sensing in mitochondria (Figure 1). Zr-BTB nMOL comprising $[Zr_6O_4(OH)_4(HCO_2)_6]$ SBUs and 2,4,6-tris(4-carboxyphenyl)aniline (BTB-NH_2) ligands was postsynthetically functionalized with GSH-selective (2*E*)-1-(2′-naphthyl)-3-(4-carboxyphenyl)-2-propen-1-one (NA) via exchanging capping groups on SBUs and conjugated with pH-sensitive fluorescein isothiocyanate (FITC) and GSH/pH-independent rhodamine-B isothiocyanate (RITC) to BTB-NH_2 ligands to afford NA@Zr-BTB/F/R. Fluorimetry and confocal laser scanning microscopy (CLSM) studies demonstrated NA@Zr-BTB/F/R as a reliable and accurate ratiometric sensor for GSH and pH in mitochondria.

BTB-NH_2 was synthesized by Suzuki coupling between *p*-ethoxycarbonylphenyl boronic acid and 2,4,6-tribromoaniline followed by base-catalyzed hydrolysis.[27] NA was prepared by aldol condensation between 2-acetonaphthone and 4-formylbenzoic acid (Figures S1–4).[28] NA itself exhibits weak fluorescence at 440 nm, but selective recognition between NA and GSH via the irreversible Michael addition reaction causes a large fluorescence increase (Figures S5–7).[29]

Received: November 9, 2020
Published: January 15, 2021

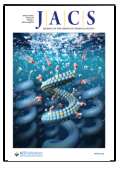

https://dx.doi.org/10.1021/jacs.0c11764
J. Am. Chem. Soc. 2021, 143, 1284–1289

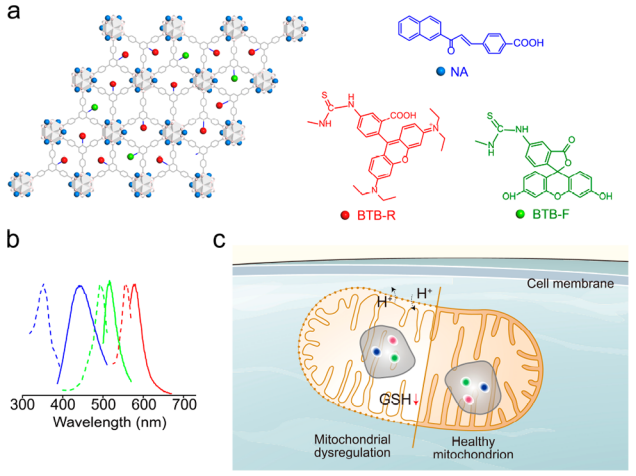

Figure 1. (a) Schematic showing NA@Zr-BTB/F/R with NA capping the Zr_6 SBUs and FITC and RITC covalently linked to the BTB-NH_2 ligands. (b) Excitation spectra (dotted lines) and emission spectra (solid lines) of NA@Zr-BTB/F/R after incubation with 10 mM GSH at 37 °C for 15 min at the NA (blue), FITC (green), and RITC (red) channels. (c) Cationic NA@Zr-BTB/F/R ratiometrically senses dysregulated mitochondria with GSH depletion and matrix acidification.

Zr-BTB nMOL was solvothermally synthesized by heating a DMF solution of $ZrCl_4$ and BTB-NH_2 at 80 °C for 24 h with formic acid (FA) and H_2O as modulators (Figure S8). The 6-connected Zr_6 SBUs are linked by 3-connected BTB-NH_2 ligands to form an infinite 3,6-connected network of $Zr_6(\mu_3\text{-}O)_4(\mu_3\text{-}OH)_4(HCO_2)_6$(BTB-$NH_2)_2$ with Kagome topology. The formulation of Zr-BTB nMOL was supported by thermogravimetric analysis (Figure S10). The monolayer morphology of Zr-BTB was demonstrated by transmission electron microscopy (TEM, Figure 2a) showing a diameter of ~180 nm and atomic force microscopy (AFM, Figure 2c,d) giving a thickness of ~1.5 ± 0.1 nm. This thickness is consistent with the modeled height of FA-terminated Zr_6 clusters. The proposed structure was confirmed by its similar powder X-ray diffraction (PXRD) pattern to that simulated for Hf_6-BTB MOL[30] (Figure 2e) and high resolution TEM (HRTEM) image along with its fast Fourier transform (FFT, Figure 2b) showing lattice fringes and a distance of ~2.0 nm between adjacent spots expected for a 3,6-connected network.

NA@Zr-BTB was synthesized by treating Zr-BTB with an excess amount of NA in water at 25 °C for 12 h. ^{1}H NMR analysis of digested NA@Zr-BTB indicated replacement of up to 84 mol % of FA by NA (Figures S9 and S11). FITC and RITC were then covalently attached to NA@Zr-BTB via forming BTB-F (BTB-NH_2 and FITC) and BTB-R (BTB-NH_2 and RITC) thiourea linkages to afford NA@Zr-BTB/F/R with the formula of $Zr_6(\mu_3\text{-}O)_4(\mu_3\text{-}OH)_4(HCO_2)_{6-m}(NA)_m$(BTB-$NH_2)_{2-x-y}$(BTB-F)$_x$(BTB-R)$_y$, where m, x, and y represent NA, FITC, and RITC loadings, respectively. NA, BTB-R, and BTB-F moieties in NA@Zr-BTB/F/R were confirmed by the presence of characteristic UV−vis absorptions of free dyes (Figure S18a) as well as the observation of $[NA + H]^+$, $[BTB\text{-}F + H]^+$, and $[BTB\text{-}R]^+$ peaks in the high-resolution mass spectra (HRMS) of digested NA@Zr-BTB/F/R (Figure S12a). TEM and PXRD showed that NA@Zr-BTB/F/R retained the morphology and crystallinity of Zr-BTB (Figure S13). NA, FITC, and RITC loadings were optimized to be 84 mol % (relative to FA), 21 mol % (relative to BTB-NH_2), and

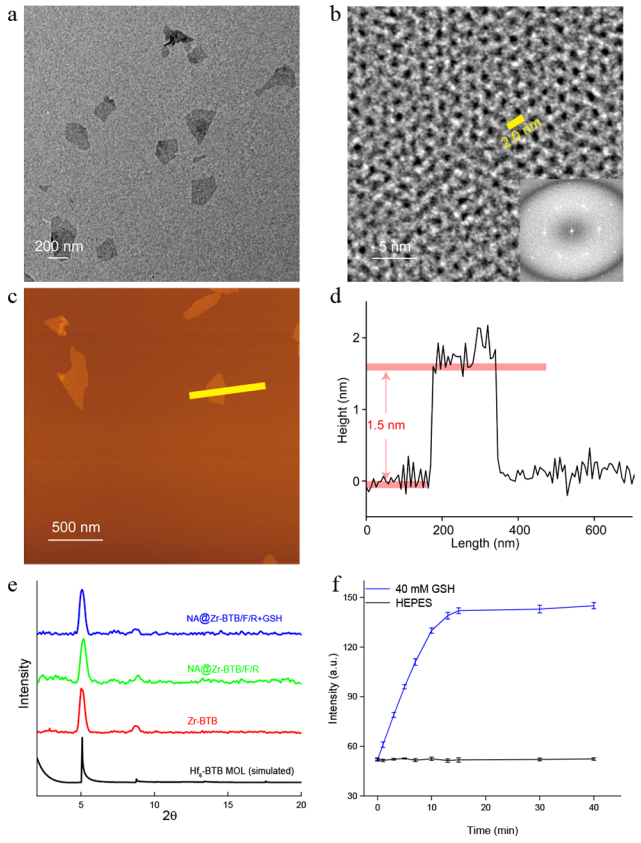

Figure 2. (a) TEM image, (b) HRTEM image with the FFT pattern in the inset, (c) AFM topography, and (d) height profile of Zr-BTB. (e) PXRD patterns of Zr-BTB and NA@Zr-BTB/F/R, freshly prepared or incubated with 40 mM GSH at 37 °C for 4 h, in comparison to the simulated pattern for the Hf_6−BTB MOL. (f) Time-dependent fluorescence responses for NA@Zr-BTB/F/R incubated with 40 mM GSH or HEPES (mean ± SD, n = 3).

74 mol % (relative to BTB-NH_2), respectively, to achieve comparable luminescence intensities for NA, FITC, and RITC and mitochondrial targeting capability (Tables S1 and S2). Dynamic light scattering (DLS) measurements showed Z-averaged diameters of 165.3 ± 3.8 and 162.2 ± 2.0 nm for Zr-BTB/R and NA@Zr-BTB/F/R, respectively (Figure S14). DLS measurements supported the stability of NA@Zr-BTB/F/R in HEPES and 0.1× PBS (Figure S15). Incubation of NA@Zr-BTB/F/R in HEPES or 0.1× PBS for 4 h dissociated <2.4% of dyes/Zr (Figure S16). The time-dependent fluorescence response of NA@Zr-BTB/F/R after GSH addition displayed a rapid enhancement which plateaued within 15 min (Figure 2f). NA@Zr-BTB/F/R was highly selective toward GSH. Thirteen different analytes including HEPES, GSH, cysteine, homocysteine, Na_2SO_3, H_2O_2, isoleucine, alanine, histidine, glutamic acid, tyrosine, lysine, and glycine were examined, but only GHS caused a drastic increase in the NA/R fluorescence intensity ratio (Figure S17).

NA@Zr-BTB/F/R was designed for ratiometric GSH sensing based on the fluorescence ratio of GSH-selective NA to GSH-independent RITC ($r_{NA/R}$) and for pH sensing based on the fluorescence ratio of pH-sensitive FITC to pH-independent RITC ($r_{F/R}$). Calibration curves and live cell sensing were performed using excitation/emission wavelengths of 352/443, 493/516, and 557/600 nm for NA, FITC, and RITC, respectively (Figure S22). NA@Zr-BTB/F/R was

https://dx.doi.org/10.1021/jacs.0c11764
J. Am. Chem. Soc. 2021, 143, 1284−1289

incubated in HEPES with GSH concentrations of 0, 1, 5, 10, 20, 30, and 40 mM and pH values of 5.04, 5.74, 6.06, 6.49, 6.97, 7.4, and 7.98. The fluorescence signals of NA, FITC, and RITC in NA@Zr-BTB/F/R were collected by a fluorimeter (Figure S23). NA responded only to GSH, FITC responded only to pH, while RITC did not respond to either GSH or pH. At pH 7.4 with different GSH concentrations, NA@Zr-BTB/F/R showed significantly increased NA signals but constant FITC and RITC signals (Figure 3a,b). On the other hand,

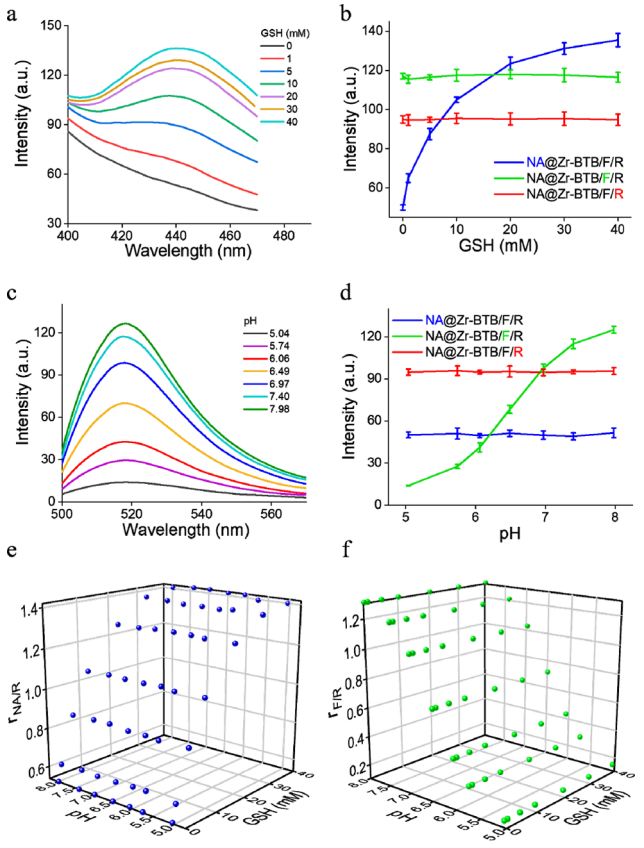

Figure 3. (a) NA emission spectra of NA@Zr-BTB/F/R with different GSH concentrations at pH 7.4. (b) NA, FITC, and RITC fluorescence intensities of NA@Zr-BTB/F/R acquired by a fluorimeter at different GSH concentrations (n = 3). (c) FITC emission spectra of NA@Zr-BTB/F/R at different pH values with 0 mM GSH. (d) NA, FITC, and RITC fluorescence intensities of NA@Zr-BTB/F/R acquired by a fluorimeter at different pH values (n = 3). Ratios of NA fluorescence over RITC fluorescence (e) and FITC fluorescence over RITC fluorescence (f) for NA@Zr-BTB/F/R. These ratios serve as calibration curves for GSH and pH sensing, respectively.

NA@Zr-BTB/F/R exhibited increased FITC signals but constant NA and RITC signals at different pH values without GSH (Figure 3c,d). GSH and pH calibration curves were then established for NA@Zr-BTB/F/R using the fluorescence ratios in Figure 3e,f. The ratiometric calibration curves for GSH and pH were empirically constructed by fitting the dependence of $r_{NA/R}$ on GSH concentration (C) according to eq 1 (R^2 = 0.999, Figure S24a) and the dependence of $r_{F/R}$ on pH according to eq 2 (R^2 = 0.996, Figure S24b), respectively. The fluorescence ratios determined by CLSM imaging also quantitatively agreed with preset GSH concentrations and pH values (Figure S25).

$$r_{NA/R} = 0.526 + 0.140(1 - e^{-c/0.788}) + 0.792(1 - e^{-c/12.694}) \quad (1)$$

$$r_{F/R} = \frac{4.213 \times 10^{-7} + 0.105e^{-2.303pH}}{3.123 \times 10^{-7} + e^{-2.303pH}} \quad (2)$$

The stability of NA@Zr-BTB/F/R under physiological conditions was verified by the unchanged PXRD pattern after incubation with 40 mM GSH at 37 °C for 4 h (Figure 2e). The highly positive ζ potentials of Zr-BTB/R (35.77 ± 0.95 mV) and NA@Zr-BTB/F/R (31.90 ± 2.95 mV) facilitated their cellular uptake (Figure S26). NA@Zr-BTB/F/R did not show any cytotoxicity at up to 300 μM Zr against cisplatin-sensitive and cisplatin-resistant human ovarian carcinoma cells A2780 and A2780cis using the MTS assay (Figure S27). Time-dependent endo/lysosomal escape was monitored by incubating A2780 cells with Zr-BTB/R for preset time intervals (Figure S28). Within the first 2 h, the enhanced red signals of Zr-BTB/R were mostly colocalized with green signals representing endo/lysosomes with Pearson's coefficients higher than 0.478, suggesting rapid endocytosis. However, the majority of Zr-BTB/R has escaped from endo/lysosomes with a Pearson's coefficient of <0.022 at 4 h. We then studied nMOL subcellular localization in greater detail by incubating A2780 cells with Zr-BTB/R for 4 h. Zr-BTB/R primarily accumulated in mitochondria with no colocalization with endoplasmic reticulum and endo/lysosomes (Figures 4a–c and S29). As NA@Zr-BTB/F/R could not be studied by CLSM colocalization analysis owing to its spectral overlap with commercial MitoTracker, we extracted mitochondria[31] and

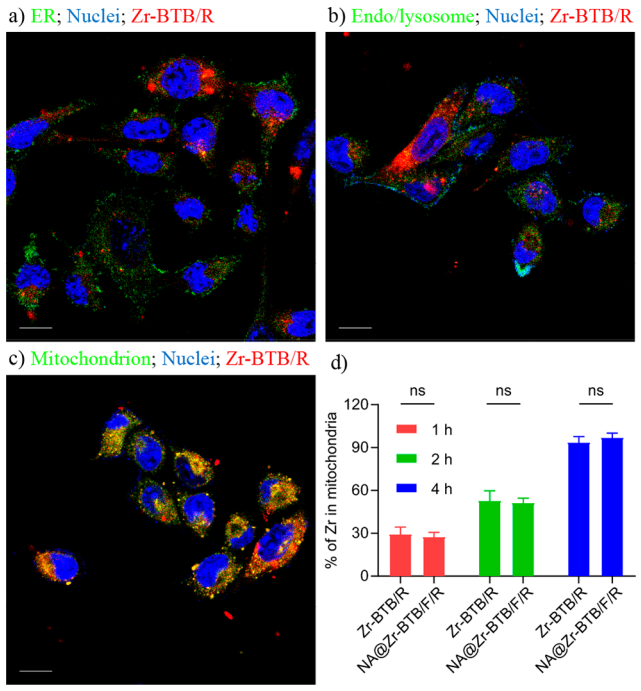

Figure 4. (a–c) Subcellular localization of Zr-BTB/R (red) in A2780 cells after incubation for 4 h. Nuclei were stained with DAPI (blue). Endoplasmic reticulum (ER), endo/lysosomes, and mitochondria were stained with ER-Tracker (green), LysoTracker (green), and MitoTracker (green), respectively. (d) Time-dependent enrichment of Zr-BTB/R and NA@Zr-BTB/F/R in mitochondria by Zr ICP-MS. The equivalent Zr concentrations are 20 μM (n = 3); ns, not significant.

https://dx.doi.org/10.1021/jacs.0c11764
J. Am. Chem. Soc. 2021, 143, 1284–1289

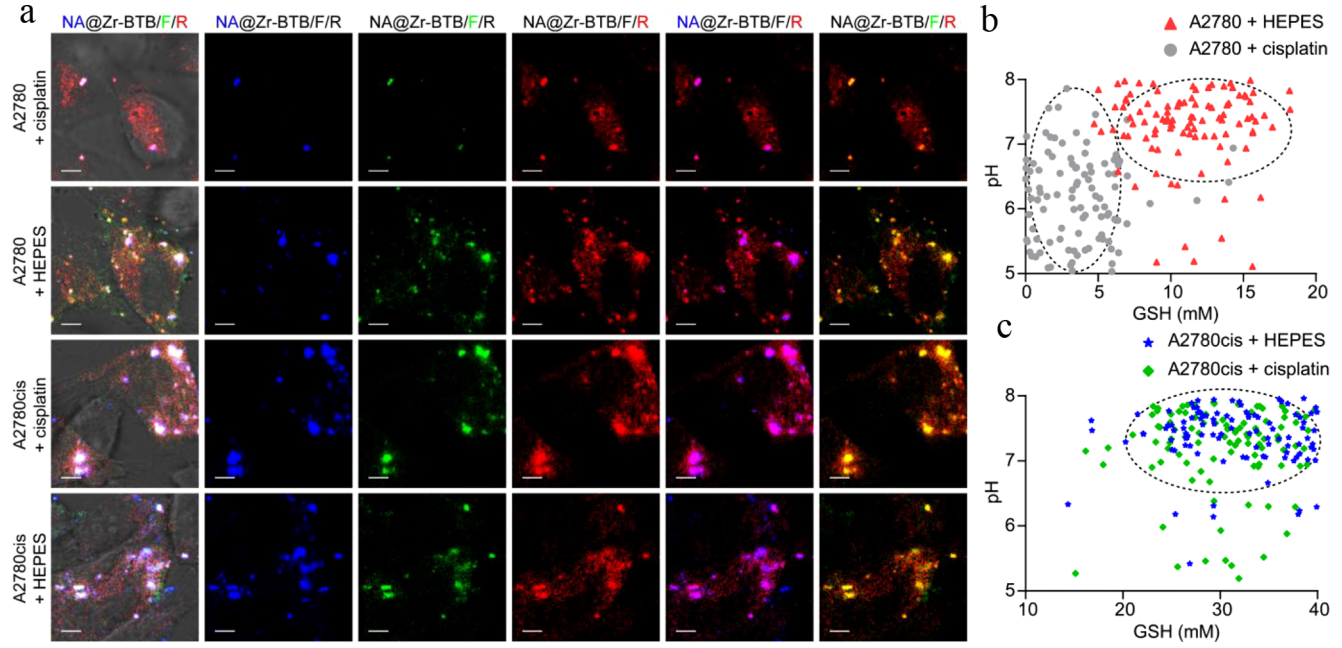

Figure 5. (a) Representative high-resolution ratiometric fluorescence imaging of cisplatin- or HEPES-treated A2780 and A2780cis cells with NA@Zr-BTB/F/R. Left to right columns: Merged NA/F/R, NA, F, R, merged NA/R, and merged F/R signals, respectively. Scale bar = 5 μm. (b, c) Scatter plots showing mitochondrial dysregulation with GSH depletion and matrix acidification as sensed by NA@Zr-BTB/F/R after incubation of (b) A2780 and (c) A2780cis cells with or without cisplatin.

determined the percentages of intramitochondrial nMOLs by ICP-MS (Figure 4d). Both Zr-BTB/R and NA@Zr-BTB/F/R with a similar RITC loading were quickly enriched in mitochondria after 4 h incubation and exhibited no difference in mitochondrial uptake in 1, 2, and 4 h. This result indicates that NA@Zr-BTB/F/R exhibits a similar mitochondrial targeting as Zr-BTB/R.

Many chemotherapeutics, including platinum drugs, induce cell death by causing mitochondrial dysregulation.[32,33] Recent studies have also pinpointed the role of mitochondrial DNA alterations on the onset of chemoresistance, which leads to redox balance alterations and signal crosstalk with nuclei, allowing a rewiring of cell metabolism.[34,35] Cisplatin-sensitive A2780 cells and cisplatin-resistant A2780cis cells were pretreated with 1 μM cisplatin and then used to evaluate the applicability of NA@Zr-BTB/F/R as a ratiometric nanosensor by CLSM (Figures 5a and S30). A2780 cells with cisplatin treatment showed dim blue and green signals of NA and FITC, indicating low GSH concentrations and pH values. In contrast, A2780 cells without cisplatin treatment presented high NA signals and FITC signals, consistent with high GSH and pH values. A2780cis cells with or without cisplatin treatment all displayed high NA and FITC signals, suggesting high GSH and neutral pH in mitochondria. NA@Zr-BTB/F/R accurately detected chemoresistance of A2780cis cells. Regions of interest (ROIs) were randomly picked from each CLSM image to obtain intensity readouts by ImageJ (Figure S31). Repeated studies showed the robustness and reproducibility of this ratiometric sensing system (Figure S32). The suitability of NA@Zr-BTB/F/R as GSH and pH sensors was confirmed in 4T1 and CT26 cells (Figure S33). Analysis of 100 ROIs for each condition revealed that mitochondrial dysregulation with GSH depletion and matrix acidification occurred only in cells at late-apoptosis (Figure 5b, c).[36−38]

In summary, we constructed the first nMOL for simultaneous GSH and pH sensing. Replacement of FA groups on the Zr_6 SBUs with NA groups and covalent conjugation of FITC and RITC to the BTB-NH_2 ligands afforded NA@Zr-BTB/F/R as a mitochondria-targeted ratiometric nanosensor for monitoring of GSH and pH independently in live cells. Cellular imaging using CLSM revealed the quantitative evidence of mitochondrial dysregulation with GSH depletion and matrix acidification. This work should inspire the development of nMOL-based ratiometric biosensors for other biological analytes and for providing new insights into pathophysiological conditions at the cellular level.

■ ASSOCIATED CONTENT

Supporting Information

The Supporting Information is available free of charge at https://pubs.acs.org/doi/10.1021/jacs.0c11764.

Synthesis and characterization of nMOLs, luminescence analysis, and *in vitro* sensing of mitochondrial dysregulation (PDF)

■ AUTHOR INFORMATION

Corresponding Author

Wenbin Lin − *Department of Chemistry and Department of Radiation and Cellular Oncology and Ludwig Center for Metastasis Research, The University of Chicago, Chicago, Illinois 60637, United States;* orcid.org/0000-0001-7035-7759; Email: wenbinlin@uchicago.edu

Authors

Xiang Ling − *Department of Chemistry, The University of Chicago, Chicago, Illinois 60637, United States*

Deyan Gong − *Department of Chemistry, The University of Chicago, Chicago, Illinois 60637, United States; Key Laboratory of Nonferrous Metal Chemistry and Resources Utilization of Gansu Province and State Key Laboratory of Applied Organic Chemistry, College of Chemistry and*

https://dx.doi.org/10.1021/jacs.0c11764
J. Am. Chem. Soc. 2021, 143, 1284−1289

Chemical Engineering, Lanzhou University, Lanzhou 730000, China

Wenjie Shi − *Department of Chemistry, The University of Chicago, Chicago, Illinois 60637, United States*

Ziwan Xu − *Department of Chemistry, The University of Chicago, Chicago, Illinois 60637, United States*

Wenbo Han − *Department of Chemistry, The University of Chicago, Chicago, Illinois 60637, United States*

Guangxu Lan − *Department of Chemistry, The University of Chicago, Chicago, Illinois 60637, United States;* orcid.org/0000-0002-0415-5849

Youyou Li − *Department of Chemistry, The University of Chicago, Chicago, Illinois 60637, United States*

Wenwu Qin − *Key Laboratory of Nonferrous Metal Chemistry and Resources Utilization of Gansu Province and State Key Laboratory of Applied Organic Chemistry, College of Chemistry and Chemical Engineering, Lanzhou University, Lanzhou 730000, China;* orcid.org/0000-0002-9782-6647

Complete contact information is available at: https://pubs.acs.org/10.1021/jacs.0c11764

Author Contributions

#X.L. and D.G. contributed equally.

Notes

The authors declare no competing financial interest.

■ ACKNOWLEDGMENTS

We thank Xiaomin Jiang for experimental help. We acknowledge the National Cancer Institute (U01-CA198989 and 1R01CA253655) and the University of Chicago Medicine Comprehensive Cancer Center (NIHCCSG: P30 CA014599) for funding support. D.G. and W.S. acknowledge financial support from the China Scholarship Council.

■ REFERENCES

(1) Zamzami, N.; Kroemer, G. The mitochondrion in apoptosis: How pandora's box opens. *Nat. Rev. Mol. Cell Biol.* **2001**, *2*, 67−71.

(2) Bock, F. J.; Tait, S. W. G. Mitochondria as multifaceted regulators of cell death. *Nat. Rev. Mol. Cell Biol.* **2020**, *21*, 85−100.

(3) Green, D. R.; Galluzzi, L.; Kroemer, G. Metabolic control of cell death. *Science* **2014**, *345*, 1250256.

(4) Jiang, N.; Fan, J. L.; Xu, F.; Peng, X. J.; Mu, H. Y.; Wang, J. Y.; Xiong, X. Q. Ratiometric fluorescence imaging of cellular polarity: Decrease in mitochondrial polarity in cancer cells. *Angew. Chem., Int. Ed.* **2015**, *54*, 2510−2514.

(5) Griffith, O. W.; Meister, A. Origin and turnover of mitochondrial glutathione. *Proc. Natl. Acad. Sci. U. S. A.* **1985**, *82*, 4668−4672.

(6) Vyas, S.; Zaganjor, E.; Haigis, M. C. Mitochondria and cancer. *Cell* **2016**, *166*, 555−566.

(7) Traverso, N.; Ricciarelli, R.; Nitti, M.; Marengo, B.; Furfaro, A. L.; Pronzato, M. A.; Marinari, U. M.; Domenicotti, C. Role of glutathione in cancer progression and chemoresistance. *Oxid. Med. Cell. Longevity* **2013**, *2013*, 972913.

(8) Matsuyama, S.; Llopis, J.; Deveraux, Q. L.; Tsien, R. Y.; Reed, J. C. Changes in intramitochondrial and cytosolic ph: Early events that modulate caspase activation during apoptosis. *Nat. Cell Biol.* **2000**, *2*, 318−325.

(9) Santo-Domingo, J.; Demaurex, N. The renaissance of mitochondrial ph. *J. Gen. Physiol.* **2012**, *139*, 415−423.

(10) Furukawa, H.; Cordova, K. E.; O'Keeffe, M.; Yaghi, O. M. The chemistry and applications of metal-organic frameworks. *Science* **2013**, *341*, 1230444.

(11) He, C. B.; Liu, D. M.; Lin, W. B. Nanomedicine applications of hybrid nanomaterials built from metal-ligand coordination bonds: Nanoscale metal-organic frameworks and nanoscale coordination polymers. *Chem. Rev.* **2015**, *115*, 11079−11108.

(12) Simon-Yarza, T.; Mielcarek, A.; Couvreur, P.; Serre, C. Nanoparticles of metal-organic frameworks: On the road to in vivo efficacy in biomedicine. *Adv. Mater.* **2018**, *30*, 1707365.

(13) Horcajada, P.; Gref, R.; Baati, T.; Allan, P. K.; Maurin, G.; Couvreur, P.; Ferey, G.; Morris, R. E.; Serre, C. Metal-organic frameworks in biomedicine. *Chem. Rev.* **2012**, *112*, 1232−1268.

(14) Hu, Z. C.; Deibert, B. J.; Li, J. Luminescent metal-organic frameworks for chemical sensing and explosive detection. *Chem. Soc. Rev.* **2014**, *43*, 5815−5840.

(15) He, C. B.; Lu, K. D.; Lin, W. B. Nanoscale metal-organic frameworks for real-time intracellular ph sensing in live cells. *J. Am. Chem. Soc.* **2014**, *136*, 12253−12256.

(16) Xu, R. Y.; Wang, Y. F.; Duan, X. P.; Lu, K. D.; Micheroni, D.; Hu, A. G.; Lin, W. B. Nanoscale metal-organic frameworks for ratiometric oxygen sensing in live cells. *J. Am. Chem. Soc.* **2016**, *138*, 2158−2161.

(17) Cui, Y. J.; Yue, Y. F.; Qian, G. D.; Chen, B. L. Luminescent functional metal-organic frameworks. *Chem. Rev.* **2012**, *112*, 1126−1162.

(18) Rabone, J.; Yue, Y. F.; Chong, S. Y.; Stylianou, K. C.; Bacsa, J.; Bradshaw, D.; Darling, G. R.; Berry, N. G.; Khimyak, Y. Z.; Ganin, A. Y.; Wiper, P.; Claridge, J. B.; Rosseinsky, M. J. An adaptable peptide-based porous material. *Science* **2010**, *329*, 1053−1057.

(19) Morris, W.; Briley, W. E.; Auyeung, E.; Cabezas, M. D.; Mirkin, C. A. Nucleic acid-metal organic framework (mof) nanoparticle conjugates. *J. Am. Chem. Soc.* **2014**, *136*, 7261−7264.

(20) Levine, D. J.; Runcevski, T.; Kapelewski, M. T.; Keitz, B. K.; Oktawiec, J.; Reed, D. A.; Mason, J. A.; Jiang, H. Z. H.; Colwell, K. A.; Legendre, C. M.; FitzGerald, S. A.; Long, J. R. Olsalaiine-based metal-organic frameworks as biocompatible platforms for h2 adsorption and drug delivery. *J. Am. Chem. Soc.* **2016**, *138*, 10143−10150.

(21) Zheng, X. H.; Wang, L.; Pei, Q.; He, S. S.; Liu, S.; Xie, Z. G. Metal-organic framework@porous organic polymer nanocomposite for photodynamic therapy. *Chem. Mater.* **2017**, *29*, 2374−2381.

(22) Foucault-Collet, A.; Gogick, K. A.; White, K. A.; Villette, S.; Pallier, A.; Collet, G.; Kieda, C.; Li, T.; Geib, S. J.; Rosi, N. L.; Petoud, S. Lanthanide near infrared imaging in living cells with yb^{3+} nano metal organic frameworks. *Proc. Natl. Acad. Sci. U. S. A.* **2013**, *110*, 17199−17204.

(23) Wang, B.; Wang, P. L.; Xie, L. H.; Lin, R. B.; Lv, J.; Li, J. R.; Chen, B. L. A stable zirconium based metal-organic framework for specific recognition of representative polychlorinated dibenzo-p-dioxin molecules. *Nat. Commun.* **2019**, *10*, 3861.

(24) Miller, S. E.; Teplensky, M. H.; Moghadam, P. Z.; Fairen-Jimenez, D. Metal-organic frameworks as biosensors for luminescence-based detection and imaging. *Interface Focus* **2016**, *6*, 20160027.

(25) Tissot, A.; Kesse, X.; Giannopoulou, S.; Stenger, I.; Binet, L.; Riviere, E.; Serre, C. A spin crossover porous hybrid architecture for potential sensing applications. *Chem. Commun.* **2019**, *55*, 194−197.

(26) Lan, G. X.; Ni, K. Y.; You, E.; Wang, M. L.; Culbert, A.; Jiang, X. M.; Lin, W. B. Multifunctional nanoscale metal-organic layers for ratiometric ph and oxygen sensing. *J. Am. Chem. Soc.* **2019**, *141*, 18964−18969.

(27) Fu, H. R.; Zhang, J. Selective sorption of light hydrocarbons on a family of metal-organic frameworks with different imidazolate pillars. *Inorg. Chem.* **2016**, *55*, 3928−3932.

(28) Chiaradia, L. D.; Martins, P. G. A.; Cordeiro, M. N. S.; Guido, R. V. C.; Ecco, G.; Andricopulo, A. D.; Yunes, R. A.; Vernal, J.; Nunes, R. J.; Terenzi, H. Synthesis, biological evaluation, and molecular modeling of chalcone derivatives as potent inhibitors of mycobacterium tuberculosis protein tyrosine phosphatases (ptpa and ptpb). *J. Med. Chem.* **2012**, *55*, 390−402.

(29) Chao, J.; Duan, Y.; Zhang, Y.; Huo, F.; Yin, C. Turn-on" fluorescence probe for selective recognition of endogenous and exogenous cysteine in cells. *J. Mol. Struct.* **2020**, *1219*, 128629.

(30) Lan, G. X.; Ni, K. Y.; Xu, R. Y.; Lu, K. D.; Lin, Z. K.; Chan, C.; Lin, W. B. Nanoscale metal-organic layers for deeply penetrating x-ray-induced photodynamic therapy. *Angew. Chem., Int. Ed.* **2017**, *56*, 12102−12106.
(31) Rambold, A. S.; Kostelecky, B.; Elia, N.; Lippincott-Schwartz, J. Tubular network formation protects mitochondria from autophagosomal degradation during nutrient starvation. *Proc. Natl. Acad. Sci. U. S. A.* **2011**, *108*, 10190−10195.
(32) Kelland, L. The resurgence of platinum-based cancer chemotherapy. *Nat. Rev. Cancer* **2007**, *7*, 573−584.
(33) Park, M. S.; De Leon, M.; Devarajan, P. Cisplatin induces apoptosis in llc-pk1 cells via activation of mitochondrial pathways. *J. Am. Soc. Nephrol.* **2002**, *13*, 858−865.
(34) Marrache, S.; Pathak, R. K.; Dhar, S. Detouring of cisplatin to access mitochondrial genome for overcoming resistance. *Proc. Natl. Acad. Sci. U. S. A.* **2014**, *111*, 10444−10449.
(35) Yang, X. K.; Fraser, N.; Moll, U. M.; Basak, A.; Tsang, B. K. Akt-mediated cisplatin resistance in ovarian cancer: Modulation of p53 action on caspase-dependent mitocliondrial death pathway. *Cancer Res.* **2006**, *66*, 3126−3136.
(36) Sawers, L.; Ferguson, M. J.; Ihrig, B. R.; Young, H. C.; Chakravarty, P.; Wolf, C. R.; Smith, G. Glutathione s-transferase p1 (gstp1) directly influences platinum drug chemosensitivity in ovarian tumour cell lines. *Br. J. Cancer* **2014**, *111*, 1150−1158.
(37) Poburko, D.; Santo-Domingo, J.; Demaurex, N. Dynamic regulation of the mitochondrial proton gradient during cytosolic calcium elevations. *J. Biol. Chem.* **2011**, *286*, 11672−11684.
(38) Azarias, G.; Perreten, H.; Lengacher, S.; Poburko, D.; Demaurex, N.; Magistretti, P. J.; Chatton, J. Y. Glutamate transport decreases mitochondrial ph and modulates oxidative metabolism in astrocytes. *J. Neurosci.* **2011**, *31*, 3550−3559.

https://dx.doi.org/10.1021/jacs.0c11764
J. Am. Chem. Soc. 2021, 143, 1284−1289